Mon. Not. R. Astron. Soc. **000**, 000–000 (0000) Printed Wednesday 23rd April, 2014 (MN LATEX style file v2.2)

X-rays from Magnetically Confined Wind Shocks: Effect of Cooling-Regulated Shock Retreat

Asif ud-Doula[1⋆], Stanley Owocki[2], Richard Townsend[3], Veronique Petit[2] & David Cohen[4]

[1] *Penn State Worthington Scranton, Dunmore, PA 18512, USA.*
[2] *Department of Physics and Astronomy, Bartol Research Institute, University of Delaware, Newark, DE 19716, USA*
[3] *Department of Astronomy, University of Wisconsin-Madison, 5534 Sterling Hall, 475 N Charter Street, Madison, WI 53706, USA*
[4] *Department of Physics and Astronomy, Swarthmore College, Swarthmore, PA 19081, USA*

arXiv:1404.5336v1 [astro-ph.SR] 21 Apr 2014

00:53Wednesday 23rd April, 2014

ABSTRACT

We use 2D MHD simulations to examine the effects of radiative cooling and inverse Compton (IC) cooling on X-ray emission from magnetically confined wind shocks (MCWS) in magnetic massive stars with radiatively driven stellar winds. For the standard dependence of mass loss rate on luminosity $\dot{M} \sim L^{1.7}$, the scaling of IC cooling with L and radiative cooling with $\dot{M}$ means that IC cooling become formally more important for lower luminosity stars. However, because the sense of the trends is similar, we find the overall effect of including IC cooling is quite modest. More significantly, for stars with high enough mass loss to keep the shocks radiative, the MHD simulations indicate a linear scaling of X-ray luminosity with mass loss rate; but for lower luminosity stars with weak winds, X-ray emission is reduced and softened by a *shock retreat* resulting from the larger post-shock cooling length, which within the fixed length of a closed magnetic loop forces the shock back to lower pre-shock wind speeds. A semi-analytic scaling analysis that accounts both for the wind magnetic confinement and this shock retreat yields X-ray luminosities that have a similar scaling trend, but a factor few higher values, compared to time-averages computed from the MHD simulations. The simulation and scaling results here thus provide a good basis for interpreting available X-ray observations from the growing list of massive stars with confirmed large-scale magnetic fields.

Key words: MHD — Stars: winds — Stars: magnetic fields — Stars: early-type — Stars: mass loss — Stars: X-rays

1 INTRODUCTION

Hot luminous, massive stars of spectral type O and B are prominent sources of X-rays thought to originate from shocks in their high-speed, radiatively driven stellar winds. In putatively single, non-magnetic O stars, the intrinsic instability of wind driving by line-scattering leads to embedded wind shocks that are thought to be the source of their relatively soft X-rays ($\sim$0.5 keV) X-ray spectrum, with a total X-ray luminosity that scales with stellar bolometric luminosity, $L_{\rm x} \sim L_{\rm bol}$ (Chlebowski et al. 1989; Nazé et al. 2011; Owocki et al. 2013). In massive binary systems the collision of the two stellar winds at up to the wind terminal speeds can lead to even higher L_x, generally with a significantly harder (up to 10 keV) spectrum (Stevens et al. 1992; Gagné 2011).

The study here examines a third source of X-rays from OB winds, namely those observed from the subset ($\sim$10%) of massive stars with strong, globally ordered (often significantly dipolar) magnetic fields (Petit et al. 2013); in this case, the trapping and channeling of the stellar wind in closed magnetic loops leads to *magnetically confined wind shocks* (MCWS) (Babel & Montmerle 1997a,b, hereafter BM97a,b), with pre-shock flow speeds that are some fraction of the wind terminal speed, resulting in intermediate energies for the shocks and associated X-rays ($\sim$2 keV). A prototypical example is provided by the magnetic O-type star θ^1 Ori C, which shows moderately hard X-ray emission with a rotational phase variation that matches well the expectations of the MCWS paradigm (Gagné et al. 2005).

Our approach here builds on our previous MHD simulation studies of the role of magnetic fields in wind channeling (ud-Doula & Owocki 2002, Paper I), including its combined effect with stellar rotation in formation of centrifugally supported magnetospheres (ud-Doula et al. 2008, Paper II) and in enhancing the angular momentum loss from the stellar wind (ud-Doula et al. 2009, Paper III). In contrast to the assumption of isothermal flow used in these

⋆ Email: asif@psu.edu

studies, our examination here of X-ray emission now requires a full treatment of the wind energy balance, including the cooling of shock-heated gas. This follows our successful specific application of MHD simulations of MCWS with a full energy balance for modeling X-ray observations of θ^1 Ori C (Gagné et al. 2005). But rather than focus on any specific star, the aim here is to derive broad scaling relations for how the X-ray luminosity and spectral properties depend on the stellar luminosity L and mass loss rate $\dot{M}$, with particular attention to how these affect the efficiency of shock cooling. The initial study here will neglect rotation, and so focus on stars with "dynamical magnetospheres" (DM), deferring to future work studies of the effect of rapid rotation on X-rays from "centrifugal magnetospheres" (CM) (Sundqvist et al. 2012; Petit et al. 2013).

For high-density winds with efficient shock cooling, the maximum shock strength depends on the speed reached before the flow from opposite footpoints of a closed loop collide near the loop top, and thus on the maximum loop height. The analyses in papers I-III show that this is generally somewhat below [see eqn. (41)] the characteristic wind Alfvén radius R_A, which for a dipole field scales as a factor $\sim \eta_*^{1/4}$ times the stellar radius R_*, where

$$\eta_* \equiv \frac{B_{eq}^2 R_*^2}{\dot{M} V_\infty} \qquad (1)$$

is the "wind magnetic confinement parameter" for an equatorial surface field B_{eq}, with $\dot{M}$ and V_∞ the wind mass loss rate and terminal speed that would occur in *non-magnetic* star with the same stellar parameters. For magnetic O-stars with $\eta_* \approx 10 - 100$, the associated Alfvén radii $R_A \approx 1.7 - 3R_*$ allow acceleration up to half terminal speed, typically about 1500 km/s. This leads to shock energies $\sim$2 keV that are sufficient to explain the moderately hard X-rays observed in θ^1 Ori C (Gagné et al. 2005).

For magnetic B-type stars, the combination of lower mass loss rates ($\dot{M} < 10^{-9} M_\odot$/yr) and very strong (1-10 kG) fields leads to very strong magnetic confinement, with $\eta_* \sim 10^4 - 10^6$ and so much larger Alfvén radii, $R_A \approx 10 - 30R_*$. This would suggest a potential to accelerate the flow to near the wind terminal speed $\sim$ 3000 km s^{-1} within closed magnetic loops, and so yield much stronger shocks (up to 10 keV) and thus much harder X-rays.

However, as illustrated schematically in figure 1 (see also figure 13 of BM97a) and quantified further below, the much lower mass loss rates of such B-stars also implies much less efficient cooling of the post-shock flow. When the associated cooling length becomes comparable to the Alfvén radius, the shock location is effectively forced to "retreat" back down the loop, to a lower radius where the lower wind speed yields a weaker shock, implying then a much softer X-ray spectrum.

To quantify this *shock retreat* effect, and derive general scalings for how the X-ray luminosity and hardness depend on the stellar luminosity and associated wind mass loss rate, the analysis here carries out an extensive parameter study based on 2D MHD simulations with a detailed energy balance. To focus on the relative roles of magnetic confinement and shock cooling, we ignore here the effects of stellar rotation, since this would introduce a third free parameter to our variations of magnetic confinement and cooling efficiency.

As a prelude to the detailed MHD simulation study in §§ 3-4, the next section (§2) develops the basic equations, and presents an analysis of the relative importance of both radiative and inverse Compton (IC) cooling in stars of various luminosities and mass loss rates. In §3, the full 2D MHD simulation results (for a standard model appropriate to O-type supergiant star with large mass loss rate and so strong radiative cooling) are used to derive differential emission measure (DEM) and associated dynamic X-ray spectra. § 4 then presents a general parameter study for how the X-ray emission in this standard model scales with a modified cooling efficiency, intended as a proxy for varying the wind mass loss rate. Comparisons with a semi-analytic scaling analysis (§4.4) indicate that X-ray luminosity depends on both the magnetic confinement parameters η_* and a radiative cooling parameter χ_∞ [see eqn. (25)], providing then a generalized scaling law [eqn. (39)] for interpreting X-ray observations for magnetic massive stars with a range of stellar parameters. The concluding section (§5) summarizes results and their implications for interpreting X-ray observations, and outlines directions of future work.

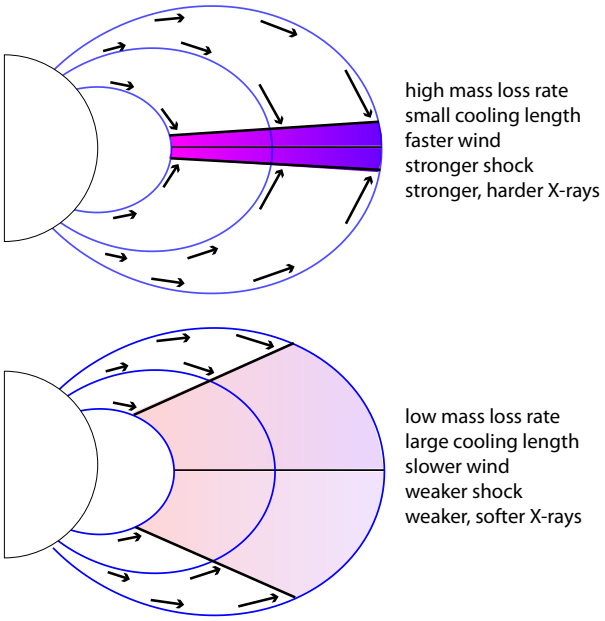

Figure 1. Schematic illustration of the "shock retreat" from inefficient cooling associated with a lower mass loss rate $\dot{M}$, showing a hemispheric, planar slice of a stellar dipole magnetic field. Wind outflow driven from opposite foot-points of closed magnetic loops is channeled into a collision near the loop top, forming magnetically confined wind shocks (MCWS). For the high $\dot{M}$ case in the upper panel, the efficient cooling keeps the shock-heated gas within a narrow cooling layer, allowing the pre-shock wind to accelerate to a high speed and so produce strong shocks with strong, relatively hard X-ray emission. For the low $\dot{M}$ case in the lower panel, the inefficient cooling forces a shock retreat down to lower radii with slower pre-shock wind, leading to weaker shocks with weaker, softer X-ray emission.

2 ENERGY BALANCE IN WIND SHOCKS

2.1 MHD equations

As in papers I-III, our general approach is to use the ZEUS-3D (Stone & Norman 1992) numerical magneto-hydrodynamics (MHD) code to evolve a 2D consistent dynamical solution for a line-driven stellar wind from a non-rotating star with a dipole surface field. In vector form, the MHD treatment includes equations for mass continuity,

$$\frac{D\rho}{Dt} + \rho \nabla \cdot \mathbf{v} = 0\,, \qquad (2)$$

and momentum balance,

$$\frac{D\mathbf{v}}{Dt} = -\frac{\nabla p}{\rho} + \frac{1}{4\pi\rho}(\nabla \times \mathbf{B}) \times \mathbf{B} - \frac{GM\hat{\mathbf{r}}}{r^2} + \mathbf{g}_{\rm lines}, \qquad (3)$$

where $D/Dt = \partial/\partial t + \mathbf{v} \cdot \nabla$ is the total time derivative advecting along the flow speed $\mathbf{v}$, and the other notation follows common conventions, as defined in detail in section 2 of Paper I. (Note that eqn. (3) here corrects some minor errors in the corresponding eqn. (2) of Paper I.)

As in all our previous MHD studies, the treatment of the acceleration $\mathbf{g}_{\rm lines}$ by line-scattering follows the standard Castor, Abbott & Klein (1975, hereafter CAK) formalism, corrected for the finite cone angle of the star, using a spherical expansion approximation for the local flow gradients (Pauldrach, Puls & Kudritzki 1986; Friend & Abbott 1986), and ignoring *non-radial* components of the line-force.

By the ideal gas law, the pressure, density and temperature are related through $p = kT/\bar{\mu}$, where k is Boltzmann's constant, and the mean molecular weight $\bar{\mu} \approx 0.62\, m_p$, with m_p the proton mass.

2.2 Energy balance

Instead of the *isothermal* approximation used in Papers I-III, we now include a full energy equation. For a monatomic ideal gas with ratio of specific heats $\gamma = 5/3$, the internal energy density is related to the pressure by $e = p/(\gamma - 1) = (3/2)p$. In analogy with the mass conservation (2), the energy balance can be written in a conservation form, but now with non-zero terms on the right-hand-side to account for the sources and sinks of energy,

$$\frac{\partial e}{\partial t} + \nabla \cdot (e\mathbf{v}) = -p\nabla \cdot \mathbf{v} + Q - C\,. \qquad (4)$$

Here the pressure term represents the effect of compressive heating ($\nabla \cdot \mathbf{v} < 0$) or expansive cooling ($\nabla \cdot \mathbf{v} > 0$), and the $Q - C$ terms account for additional volumetric heating or cooling effects. In hot-star winds, UV photoionization heating sets a floor to the wind temperature on the order the stellar effective temperature (Drew 1989), but otherwise such heating is unimportant in the shock-heated regions that are the focus of the study here. For cooling, we include here both optically thin radiative emission as well as *inverse Compton* (IC) cooling from scattering of the stellar UV photons by electrons that can be heated to keV energies in shocks.

For the analysis below, it is convenient to use the mass conservation (2) to rewrite the left side of the energy conservation (4) in terms of the total advective time derivative of the energy per unit mass e/ρ,

$$\rho \frac{D(e/\rho)}{Dt} = -p\nabla \cdot \mathbf{v} - C_{rad} - C_{\rm IC}\,. \qquad (5)$$

The volume cooling rate from radiative emission has the scaling,

$$C_{rad} = n_e n_p \Lambda(T) = \rho^2 \Lambda_m(T)\,, \qquad (6)$$

where $\Lambda(T)$ is the optically thin cooling function (MacDonald & Bailey 1981; Schure et al. 2009), and the latter equality defines a mass-weighted form $\Lambda_m \equiv \Lambda/\mu_e\mu_p$. For a fully ionized plasma the proton and electron number densities n_p and n_e are related to the mass density ρ through the associated hydrogen mass fraction $X = m_p/\mu_p = m_p n_p/\rho$ and mean mass per electron $\mu_e = \rho/n_e = 2m_p/(1+X)$. We assume here the standard solar hydrogen abundance $X = 0.72$.

The IC volume cooling rate (White & Chen 1995) scales with the electron pressure $n_e kT = (\bar{\mu}/\mu_e)p$ and the photon energy density U_{ph},

$$C_{\rm IC} = 4\sigma_e n_e kT \frac{U_{ph}}{m_e c} = 4\frac{\kappa_e \bar{\mu}}{m_e c}\, p\, U_{ph}\,, \qquad (7)$$

where m_e and c are the electron mass and speed of light, and σ_e and $\kappa_e \equiv \sigma_e/\mu_e$ are the electron scattering cross section and the associated opacity.

2.3 Characteristic time scales

Let us examine the time scales for the various processes in the energy equation (5). Dividing by the internal energy e, we can recast this energy equation in terms of processes leading to a change in temperature,

$$-\frac{1}{T}\frac{DT}{Dt} = \frac{2}{3}\nabla \cdot \mathbf{v} + \frac{2\bar{\mu}}{3k}\frac{\rho\Lambda_m(T)}{T} + \frac{8}{3}\frac{\kappa_e\bar{\mu}}{m_e c}U_{ph} \qquad (8)$$

$$-\frac{1}{t_T} = \frac{1}{t_{ad}} + \frac{1}{t_{rad}} + \frac{1}{t_{\rm IC}}\,. \qquad (9)$$

The first term on the right-hand side of (8) represents the effects of heating by adiabatic compression (if $\nabla \cdot \mathbf{v} < 0$) or cooling by adiabatic expansion (if $\nabla \cdot \mathbf{v} > 0$). For the discontinuous compression at a shock, this term leads to the sudden jump in post-shock temperature. But in a wind expansion, it nominally has a cooling effect, including in the regions of a post-shock flow. For such post-shock cooling layers, equation (9) thus identifies the timescale for change in temperature with associated cooling timescales for adiabatic expansion, radiative emission, and inverse Compton scattering.

2.4 Cooling times for a standing shock

As a basis for estimating the relative importance of these processes for MCWS, let us examine the scalings of the associated timescales for the simplified case of a steady, standing shock at a fixed radius r_s in a steady spherical wind with specified mass loss rate $\dot{M}$ and pre-shock wind speed V_w (see Owocki et al. 2013).

For a strong shock, the immediate post-shock density is a factor 4 times the pre-shock wind value, $\rho_s = 4\rho_w = 4\dot{M}/(4\pi r_s^2 V_w)$. Since the post-shock flow speed is correspondingly *reduced* by this factor 4, the net shock jump is $\Delta v = (3/4)V_w$, yielding a post-shock temperature

$$T_{\rm s} = \frac{3}{16}\frac{\bar{\mu}V_w^2}{k} \approx 14\,{\rm MK}\, V_8^2 \approx 1.2\,{\rm keV}\, V_8^2\,, \qquad (10)$$

where $V_8 \equiv V_w/(10^8 {\rm cm/s})$. If we take the post-shock speed to be roughly constant and assume, for simplicity, spherical expansion $\nabla \cdot \mathbf{v} = 2v/r = V_w/2r_s$, then we obtain for the adiabatic expansion timescale,

$$t_{ad} = 3\frac{r_s}{V_w} = 30\,{\rm ks}\,\frac{r_{12}}{V_8}\,, \qquad (11)$$

where $r_{12} = r_s/10^{12}$ cm.

We can write the radiative cooling time as

$$t_{rad} = \frac{3\pi k}{2\bar{\mu}}\,\frac{r_s^2 V_w T_s}{\dot{M}\Lambda_m(T_s)} \approx 0.75\,{\rm ks}\,\frac{V_8^3\, r_{12}^2}{\dot{M}_{-6}}\,, \qquad (12)$$

where $\dot{M}_{-6} = \dot{M}/(10^{-6} M_\odot/{\rm yr})$ and the numerical evaluation assumes a constant cooling function, $\Lambda(T_{\rm s}) \approx 4.4 \times 10^{-23}\,{\rm erg\,cm^3 s^{-1}}$, over the relevant range of shock temperatures,

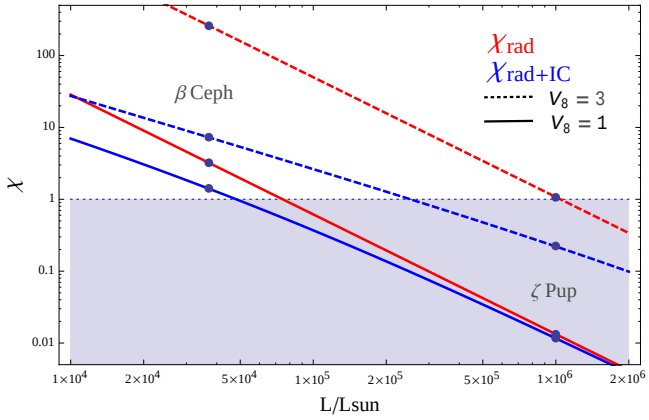

Figure 2. Cooling parameter for radiative processes (χ_{rad}; red curves) and combined radiative and inverse-Compton processes (χ_{rad+IC}; blue curves), plotted vs. stellar luminosity (in solar units $L/L_\odot$), which serves as proxy for increased mass loss rate ($\dot{M} \sim L^{1.7}$). Results are plotted for pre-shock wind speeds $V_8 = 1$ (solid line) and $V_8 = 3$ (dashed lines), with fixed radius $r_{12} = 1$. The points give values appropriate to an early B-type star like β Cephei (left) and an O-type supergiant like ζ Pup (right).

$10^{6.5}\,K < T_s < 10^{7.5}\,K$ (Schure et al. 2009). This allows us to define a radiative vs. adiabatic cooling parameter,

$$\chi_{rad} \equiv \frac{t_{rad}}{t_{ad}} = 0.025\,\frac{V_8^4\,r_{12}}{\dot{M}_{-6}}\,. \tag{13}$$

Note that this is 0.25 times the cooling parameter defined by Stevens et al. (1992) in the context of colliding stellar winds.

For stellar luminosity L, the photon energy density at shock radius r_s is

$$U_{ph} = \frac{L}{4\pi r_s^2 c}\,\frac{2}{1+\mu_*}\,, \tag{14}$$

where the factor with $\mu_* = \sqrt{1-(R_*/r_s)^2}$ corrects for the difference between energy density and flux for a star of radius R_* with uniform surface brightness (i.e., ignoring limb darkening). We then find for the IC cooling time,

$$t_{\rm IC} = \frac{3\pi m_e c^2}{2\kappa_e \bar{\mu}}\,\frac{r_s^2(1+\mu_*)}{L} \approx 2.8\,{\rm ks}\,\frac{r_{12}^2}{L_6}\,, \tag{15}$$

where $L_6 \equiv L/(10^6 L_\odot)$ and the latter approximation ignores the factor 2 variation from the $1+\mu_*$ term.

To compare the radiative and IC cooling times, let us relate the mass loss rate and luminosity through the CAK mass loss scaling. Ignoring for simplicity the dependencies on other stellar parameters like stellar mass or radius, we can approximate this as (see, e.g., §4.3 of Owocki 2004)

$$\dot{M}_{-6} \approx 3.6 L_6^{1/\alpha} \approx 3.6 L_6^{5/3}\,, \tag{16}$$

where the latter relation use a typical CAK power index $\alpha \approx 0.6$.

To examine the effect of including such IC cooling, let us now define an associated IC to adiabatic cooling time $\chi_{\rm IC} \equiv t_{\rm IC}/t_{ad}$. The total radiative + IC cooling parameter is then obtained by inverse sum of the components,

$$\frac{1}{\chi_{rad+IC}} = \frac{1}{\chi_{rad}} + \frac{1}{\chi_{\rm IC}}\,. \tag{17}$$

As an example, figure 2 plots the luminosity variation of the radiative cooling and radiative + IC cooling parameters for pre-shock wind speeds $V_8 = 1$ and $V_8 = 3$. High luminosity stars – e.g. the case of the O-supergiant ζ Puppis marked by the right-side dots – are well into the radiative regime (marked by the shading) $\chi < 1$ for both wind speeds. Moreover, the similar values of the radiative and radiative + IC curves indicate that, for such high luminosity stars, including IC processes has only a marginal additional effect on the cooling.

In contrast, for lower luminosity stars – e.g. the case of the B2-giant β Cephei – cooling is in the adiabatic regime, especially for the higher-speed case $v_8 = 3$; but the IC cooling now significantly reduces the cooling time compared to the models with just radiative cooling, which are even further in the adiabatic regime.

For this simple model of a standing shock in spherical outflow, the overall conclusion from this timescale comparison is that even strong shocks in luminous stars with large mass-loss rates should be radiatively cooled. In less luminous stars with weaker winds, IC can significantly enhance cooling over the purely radiative case, but in the lowest luminosity stars even their combined effect is less than adiabatic expansion.

For X-ray emission from MCWS that form in closed magnetic loops, it is helpful to translate these timescales to associated cooling lengths. For any post-shock cooling timescale t, the associated length scale can be approximated by its product with the post-shock flow speed, $\ell = tV_w/4$. The ratio of this cooling length to the shock radius is thus $\ell/r_s = tV_w/4r_s = (3/4)t/t_{ad} = 0.75\,\chi_{rad}$. For cases with efficient cooling, $\chi_{rad} \ll 1$, the shock radius should be a small cooling length ℓ below the loop apex near the Alfvén radius, implying $R_A \approx r_s + \ell \approx r_s(1 + 0.75\chi_{rad})$.

But for inefficient cooling cases with $\chi > 1$, the cooling length becomes comparable to the loop apex radius, forcing the shock retreat and associated shock weakening. As basis for interpreting such shock retreat effects in the MHD simulations below (§§3-4), let us next illustrate this process through an analytic scaling for this simple example of a spherical standing shock. Appendix B generalizes this to account for the curved flow geometry of material trapped in closed dipole loop.

2.5 Spherical Scaling for Cooling-Regulated Shock-Retreat

The above scaling analysis characterizes the efficiency of post-shock cooling by comparing the timescales in the immediate post-shock transition, focusing particularly on the relative values of the radiative and IC cooling to the expansion timescale assuming a *constant* post-shock speed $v = V_w/4$. More realistically, for one-dimensional flow against some fixed barrier or "wall", this post-shock speed must slow to zero at this wall, which in this simplified spherical expansion model acts as a proxy for the apex radius r_m of a given closed magnetic loop.

The issue at hand then is to derive scalings for the total length $r_m - r_s$ for the cooling layer between this apex and the shock at radius r_s. Moreover, to be self-consistent, this should take into account the radial scaling for the pre-shock wind speed. As an alternative to solving the full dynamical acceleration of outflows along such a closed magnetic loop, let us simply assume that at any given radius r, the flow speed v can be approximated by a standard "beta" velocity law,

$$v(r) = V_\infty(1 - R_*/r)^\beta \equiv V_\infty w(r)\,, \tag{18}$$

where w represents a scaled speed in terms of the terminal speed V_∞, which for simplicity we take here to have a value equal to that for the non-magnetized wind. Any flow extending to the apex radius r_m reaches a scaled speed $w_m \equiv w(r_m)$; but in general the

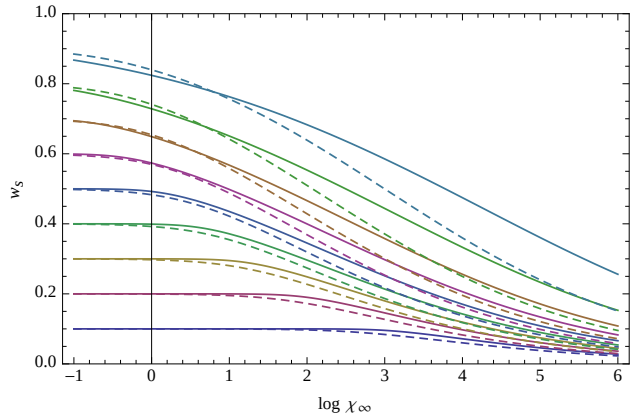

Figure 3. Reduced shock speed w_s vs. log of the cooling parameter χ_∞, plotted for various values of scaled apex speed w_m from 0.1 to 0.9. Dashed curves are for the simple spherical expansion form for shock retreat, while the solid curves account for dipole loop geometry, as described by the generalized shock-retreat analysis in Appendix B.

limited cooling implies a shock retreat to some radius $r_s \leqslant r_m$, with a reduced scaled pre-shock speed $w_s \equiv w(r_s) \leqslant w_m$. As the cooling becomes more inefficient, the larger cooling layer forces a shock retreat to a lower shock radius with a lower wind speed, for which the shocks are weaker and so have a smaller cooling length.

To derive the shock strength that results from this self-regulation by cooling-efficiency shock retreat, let us first solve for the evolution of the post-shock temperature using the steady-state form for the temperature equation (8),

$$\frac{v}{T}\frac{dT}{dr} \approx \frac{2}{3}\frac{v}{\rho}\frac{d\rho}{dr} - \frac{2\bar{\mu}}{3k}\frac{\rho\Lambda_m}{T}\,, \tag{19}$$

where for simplicity we have neglected IC cooling. Here we have used the steady-state mass continuity to rewrite the adiabatic cooling in terms of the velocity and density. Since the post-shock flow is by definition subsonic, we can approximate it as nearly *isobaric*, implying that $\rho T \approx \rho_s T_s$, where the post-shock temperature is given by eqn. (10) and the post-shock density by $\rho_s = 4\rho_w = \dot{M}/(\pi V_w(r_s) r_s^2)$. Using this and the mass continuity to eliminate both the speed v and density ρ in favor of the temperature T, we can combine the adiabatic cooling with the advection along the temperature gradient, leading to a simple first-order differential equation for the post-shock temperature,

$$\frac{T^2}{r^2}\frac{dT}{dr} = -\frac{4/5}{\chi_{rad}}\frac{T_s^3}{r_s^3}\,, \tag{20}$$

where the factor $4/5$ adjusts for constants used in the above definition (13) for the cooling parameter χ_{rad} associated with the cooling time from an assumed adiabatic expansion. With the boundary condition $T(r_s) = T_s$, eqn. (20) can be trivially integrated to give an explicit solution for temperature in the post-shock region[1],

$$T(r) = T_s\left[\frac{4/5}{\chi_{rad}}\left(1 - \left(\frac{r}{r_s}\right)^3\right) + 1\right]^{1/3}\,. \tag{21}$$

[1] For simplicity, this assumes a constant cooling parameter Λ_m. It is trivial to extend the analysis to a power-law temperature variation. For example, the rough fit $\Lambda_m \sim T^{-1/2}$ gives a scaling in which the exponent value $1/3$ in the derived solution (21) is replaced by $2/7 = 1/3.5$.

Identifying the loop apex radius r_m as a barrier location where the temperature formally drops to zero, $T(r_m) \equiv 0$, we find[2]

$$\frac{r_m}{r_s} = \left(1 + \frac{5\chi_{rad}}{4}\right)^{1/3}\,. \tag{22}$$

We can readily turn this around to solve for the shock radius, accounting for the fact that, from (13), $\chi_{rad} \sim r_s V_w^4(r_s)$. Assuming a simple $\beta = 1$ velocity law (18), we find

$$\left(\frac{r_m}{r_s}\right)^3 = 1 + \chi_\infty \frac{r_s}{R_*}\left(1 - \frac{R_*}{r_s}\right)^4\,, \tag{23}$$

which alternatively can be cast as an equation for the scaled shock speed w_s,

$$\left(\frac{1-w_s}{1-w_m}\right)^3 = 1 + \chi_\infty \frac{w_s^4}{1-w_s}\,. \tag{24}$$

Here we have defined a cooling parameter associated with the terminal speed, $v = V_\infty$, evaluated at the stellar radius R_*, while also absorbing the $5/4$ factor,

$$\chi_\infty \equiv \frac{15\pi}{128}\frac{V_\infty^4 R_*}{\dot{M}\Lambda_m} \approx 0.034\,\frac{V_8^4\, R_{12}}{\dot{M}_{-6}}\,. \tag{25}$$

The numerical evaluation uses the scaled values $V_8 \equiv V_\infty/(10^8 \text{cm/s})$ and $R_{12} \equiv R_*/10^{12}$ cm. For typical values $V_8 = 3$ and $R_{12} = 1$, $\chi_\infty = 1$ corresponds to a wind mass loss rate $\dot{M}_{-6} \approx 0.8$. Comparison with eqn. (13) for χ_{rad} shows a superficially similar scaling to (25) for χ_∞; but it is important to note that χ_{rad} represents a comparison between radiative to adiabatic timescales at some *local* shock radius r_s, while χ_∞ is a fixed *global* characteristic of the star that controls the spatial shock retreat.

Given χ_∞, and the apex speed w_m, eqn. (24) can be readily solved for w_s by standard root finding. For this simple spherical example of shock retreat, the dashed curves in figure 3 plot w_s vs. $\log\chi_\infty$ for a range of w_m. The solid curves compare results for the generalization derived in Appendix B to account (though solution of eqn. (B16)) for the dipole loop geometry.

Associating the maximum loop radius with the Alfvén radius, which scales with the magnetic confinement as $R_A \sim \eta_*^{1/4}$, we can use this dipole shock retreat solution to estimate the reduction in shock temperature T_s, and thus the reduced shock energy dissipation available for X-ray emission. §5 develops this further to derive analytic scaling laws for L_x as function of η_* and χ_∞. This proves very helpful for interpreting results from the full numerical MHD models that we now describe.

3 MCWS X-RAYS FROM STANDARD MODEL

3.1 Model description and parameters

Let us now turn to our numerical simulations of shock heating and X-ray emission in MCWS. As a basis for our study of how cooling efficiency affects X-ray emission, let us first examine the X-ray

[2] Note that in the strong cooling limit $\chi_{rad} \ll 1$, this gives $r_m \approx r_s + \ell = r_s(1+5\chi_{rad}/24)$, implying a cooling length ℓ that is a factor $5/18 \approx 0.28$ smaller than the value $0.75 r_s \chi_{rad}$ predicted at the end of §2.4. This correction reflects the significant deceleration of the post-shock flow speed, with associated increases in density, both of which lead to stronger cooling and so a shorter cooling length than predicted by a simple constant-speed advection over the post-shock timescale.

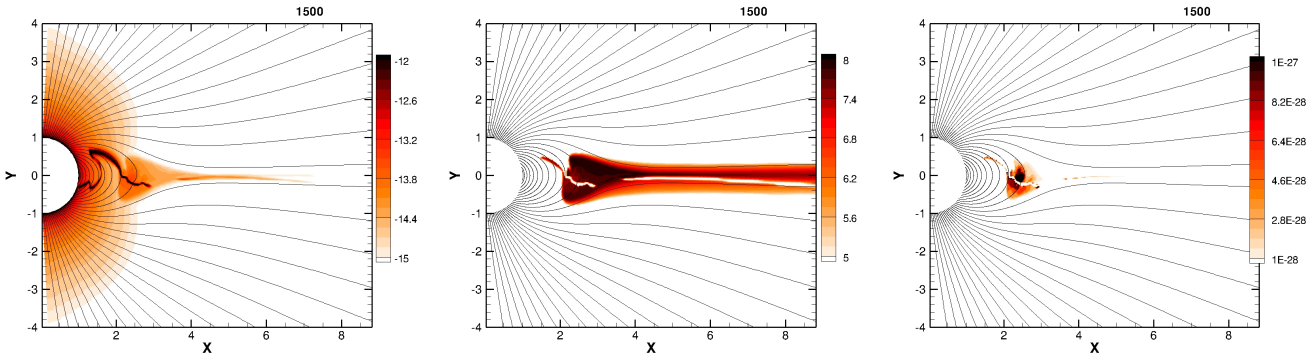

Figure 4. Color plots of log density (left) and log temperature (middle) for arbitrary snapshot of structure in the standard model with $\eta_* = 100$ and no IC cooling. The right panel plots the proxy X-ray emission XEM_{T_x} (weighted by the radius r) from (26), on a *linear* scale for a threshold X-ray temperature $T_x = 1.5\,$MK.

properties for the same standard model that formed the basis of the previous MHD parameter studies in papers I-III.

Roughly representative of an O-type supergiant star like ζ Puppis, this model assumes a radius $R_* = 19R_\odot$, luminosity $L = 10^6 L_\odot$, and an effective mass of $M = 25M_\odot$. (This reflects a factor two reduction below the Newtonian mass to account for the outward force from the electron scattering continuum.) Within the standard, finite-disk-corrected CAK model, in a non-magnetic star this leads to a mass loss rate $\dot{M} \sim 3.3 \times 10^{-6} M_\odot$/yr and wind terminal speed $V_\infty \approx 3000\,$km/s. As illustrated in fig. 2, this model is generally within the cooling regime $\chi < 1$, with IC making only a minor contribution to the overall cooling, except for high wind speeds $V_8 \sim 3$.

Our standard model assumes a magnetic confinement parameter $\eta_* = 100$, giving then an Alfvén radius $R_{\rm A}/R_* \approx \sqrt{10} \approx 3.1$. For the stellar and wind parameters quoted above, this requires a polar magnetic field of $B_p = 3\,$kG. Since these stellar and wind parameters are fixed throughout this paper, exploration of any models with different η_* is done simply by adjusting the assumed dipolar field strength by the prescription, $B_p = 300{\rm G}\sqrt{\eta_*}$. Specifically, the models below with $\eta_* = 10$ assume $B_p \approx 1000\,$G.

For all simulations here, the numerical specifications – such as the computational grid, initial condition, and boundary conditions – are as in Paper I. The initial condition introduces the dipole field of chosen strength into a relaxed steady, spherically symmetric wind driven by line-scattering of stellar radiation according to the CAK formalism. The temperature is initially set to the stellar effective temperature $T_{\rm eff}$, but now varying according to the energy equation (5) to allow for shock-heating and post-shock cooling, keeping however a floor at $T_{\rm eff}$ as a proxy for the photoionization heating by the stellar UV radiation. To average over dynamic structure associated with wind trapping and infall, the models are run to a maximum time $t_{\rm fin}$ that is many times the wind flow time $t_{\rm flow} = R_{max}V_\infty \approx 150\,$ks over the model range extending to $R_{max} = 15R_*$. For the standard model, we take $t_{\rm fin} = 3000\,$ks, but for the broader parameter study we use a common value that is half this standard, i.e., $t_{\rm fin} = 1500\,$ks. To allow for relaxation from the initial condition, all quoted time-averaged quantities here are computed starting at $t = 500\,$ks, and extending to $t_{\rm fin}$ ks.

3.2 Density and Temperature structure and associated X-ray Emission

Let us first consider a model with radiative cooling, but ignoring IC cooling, and with a moderately strong magnetic confinement $\eta_* = 100$, implying an Alfvén radius $R_A \approx 3.1R_*$. The left and middle panels of figure 4 show color plots of the characteristic spatial structure in log density and log temperature at a fixed time snapshot, chosen arbitrarily here to be half the final time $t = t_{\rm fin}/2 = 1.5\,$Ms. Note that the highest density occurs in radiatively cooled regions with low temperature (near the floor at $T \approx T_{\rm eff}$), while the shock-heated regions with temperatures up to $\log T \approx 7.5$ (K) have relatively low density.

To characterize the regions of X-ray emission, which scales with the density-squared emission measure of material that is hot enough to emit X-rays, let us define a simple proxy that weights the emission measure by a Boltzmann factor for some threshold temperature T_x,

$$X_{T_x}(\rho, T) \equiv \rho^2 \exp(-T_x/T)\,. \qquad (26)$$

The rightmost panel of figure 4 shows a color scale plot of X_{T_x} for a threshold temperature $T_x = 1.5\,$MK, sufficient to produce X-rays of $\sim$0.1 keV and above. Note that the X-ray emission is concentrated near the top of the outermost closed loop, just below the Alfvén radius, $R_A \approx 3.1R_*$. This is much more localized than the distributed regions of high temperature, which extend outward well beyond the Alfvén radius, centered on the current sheet that defines the jump in polarity for wind-opened field line on each side of the magnetic equator. While impressive in a color plot of the temperature, such extended regions have too low a density to produce much significant X-ray emission.

3.3 Radius-time plots of latitudinally integrated X-ray emission

Such snapshots do not capture the extensive dynamical variability that is inherent from the trapping and subsequent infall of material in closed magnetic loops, as can be seen by animations of the evolving structure.

To capture this here in a still graphic, let us collapse one of the spatial dimensions by latitudinally integrating this X-ray emission

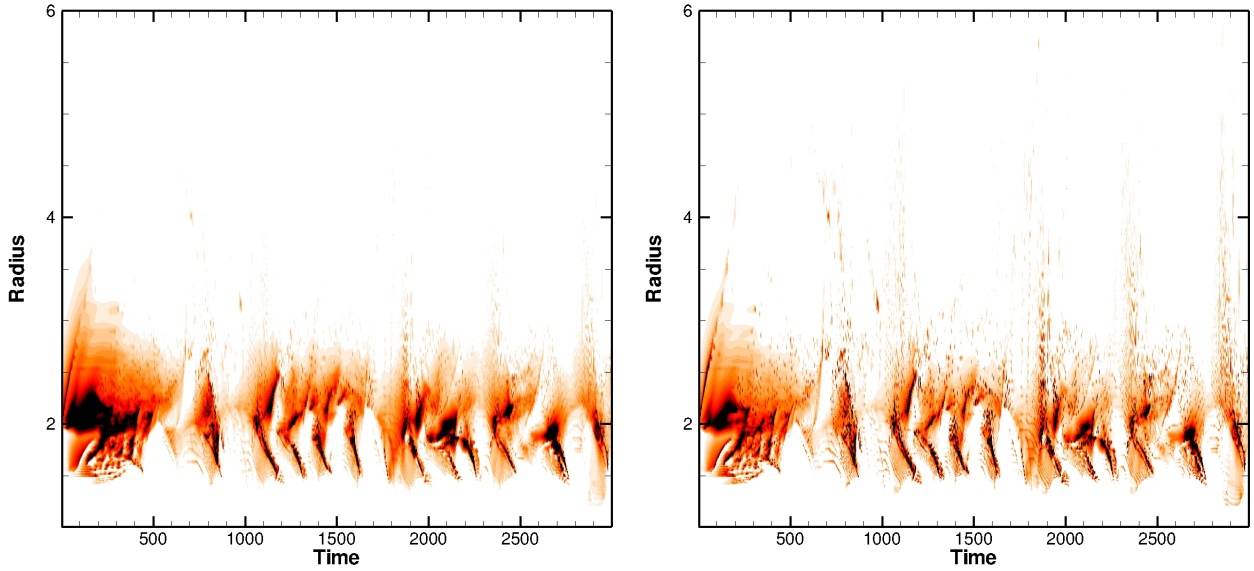

Figure 5. Radial distribution of latitudinally integrated X-ray emission above an X-ray threshold, plotted vs. radius (in R_*) and time (in ks) for the standard model. The left panel uses the Boltzmann formula (26) with T_x =1.5 MK, and right panel shows the actual energy-integrated X-ray emission above a threshold E_x = 0.3 keV.

measure XEM[3],

$$\frac{d\,\bar{X}_{T_x}}{dr}(r,t) \equiv 2\pi r^2 \int_{-\pi/2}^{\pi/2} \sin(\theta) X_{T_x}[\rho(r,\theta,t), T(r,\theta,t)]\, d\theta\,, \tag{27}$$

For this standard model with η_* =100 (and neglecting IC cooling), the left panel of figure 5 then shows color plots of the time and radius variation of this integrated XEM for the threshold temperature, T_x= 1.5MK.

The right panel shows the actual distribution of total X-ray emission above an energy threshold E_x =0.3 keV, computed using the spectral synthesis method described in the next section. The close correspondence supports the utility of the simple Boltzmann form (26) for characterizing the total X-ray emission.

But both plots provide a vivid illustration of the intrinsic time variability and spatial structure of the X-ray emission in such MHD simulation models. Quickly after the start-up condition, strong initial shocks form to produce extensive X-ray emission, centered on a radius $r \approx 2.1R_*$, but extending from $r = 1.5R_*$ up to around $r \approx 2.8R_*$, i.e. just below the Alfvén radius $R_A \approx 3.1R_*$. By $t = 500$ ks the cooling and infall of this shock-heated material leads to a brief interval of weak emission, which however recovers as new, somewhat less organized and thus somewhat less distributed shock heating with more moderate X-ray emission. This material again cools and leads to repeated cycles of shock-heated X-ray emission and low-emission infall, with quasi-regular period about 250 ks.

While quite distinctive in the 2D simulations here, in more realistic 3D models the likely phase incoherence among heating/infall cycles at different azimuths would tend to smooth out any overall variability in observed X-rays. In the 3D model computed in ud-Doula et al. (2013), for example, such azimuthal averaging greatly reduces the stochastic variations derived for Balmer line emission.

[3] This is analogous to the latitudinally integrated mass distribution defined to illustrate the r, t accumulation of equatorial mass in the rotating wind models of paper II. See figs. 4, 5, 7 and 9 there.

3.4 Dynamic spectrum

Let us now examine the dynamic X-ray spectrum that arises from this cycle of shock-heating and mass infall.

The X-ray emission at any photon energy E can be computed using the energy-dependent emission function, $\Lambda_m(E,T)$, derived from a standard plasma emission code like the APEC model (Smith et al. 2001; Foster et al. 2012) in XSPEC (Arnaud 1996).

Integration over all energies gives the total cooling function introduced in eqn. (6), $\Lambda_m(T) = \int \Lambda_m(E,T)\, dE$. The energy-dependent volume emissivity (with CGS units erg/(cm^3 s keV)) just weights this by the associated density-squared emission measure (EM) of gas at the given temperature,

$$\eta_x(E,\rho,T) = \rho^2 \Lambda_m(E,T)\,. \tag{28}$$

Integration over the full spherical volume of the model then gives (neglecting any absorption or occultation) the energy spectrum of total emitted luminosity,

$$L_x(E) = \int \Lambda_m(E,T)\rho^2\, dV \equiv \int \Lambda_m(E,T) \frac{d\,EM(T)}{d\ln T} d\ln T\,, \tag{29}$$

where the latter equality defines the volume-integrated *differential emission measure*, DEM $\equiv d\,EM(T)/d\ln T$.

The color plots in figure 6 illustrate the time variations of the DEM(t,T) (vs. $\log T$, left) and the resulting dynamic X-ray spectrum $L_x(E,t)$ (vs. $\log E$, right). Note again the dynamical variability from the trapping and subsequent infall of material in closed magnetic loops.

In these terms, the radius-time variation of total X-ray emission above a threshold, as plotted in the right panel of figure 5 for E_x =0.3 keV, is defined by

$$\frac{dL_{E_x}}{dr}(r,t) \equiv \int_{-\pi/2}^{\pi/2} r^2 \sin(\theta)\rho^2(r,\theta,t)\bar{\Lambda}_m[T(r,\theta,t), E_x]\, d\theta \tag{30}$$

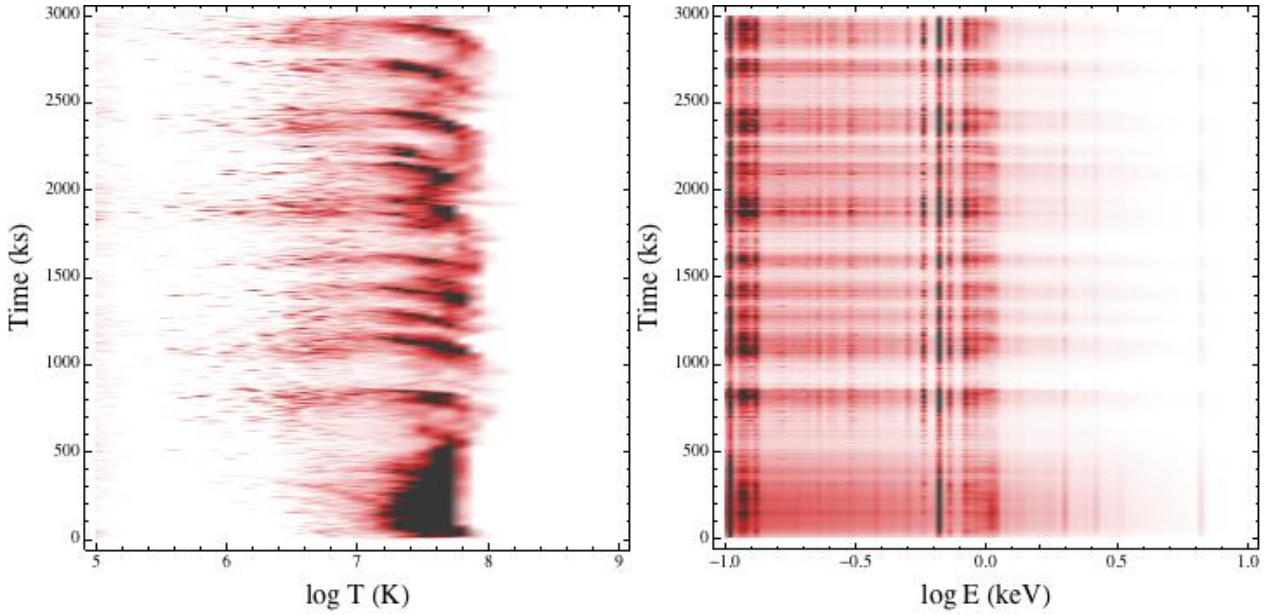

Figure 6. *Left:* Differential emission measure, $DEM(t,T)$, plotted with a linear color scale versus time t (in ks) and log temperature $\log T$ (in K) for the standard model without IC cooling. *Right:* Associated dynamic X-ray spectrum $L_x(E,t)$, plotted with a linear color scale vs. time and $\log E$ (in keV).

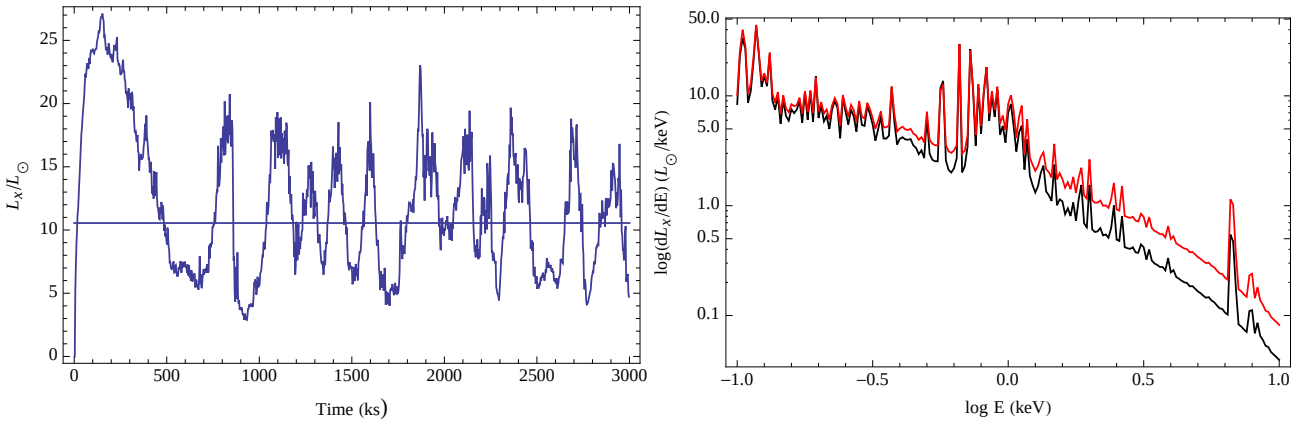

Figure 7. *Left:* For standard model simulations with $\eta_* = 100$, the time variation of cumulative X-ray luminosity $L_x(E > E_x, t)$ above X-ray threshold energy E_x=0.3 keV, plotted in units of $L_\odot$. The horizontal line shows the time-averaged value $L_x \approx 67 L_\odot$, computed over times $t > 500$ ks, after the model has relaxed from its initial condition. *Right:* Log scale of time-averaged X-ray spectrum dL_x/dE vs. $\log E$. The black and red curves compare results with and without IC cooling.

where

$$\bar{\Lambda}_m(T, E_x) \equiv \int_{E_x}^{\infty} \Lambda_m(E,T)\, dE \qquad (31)$$

defines a spectrally integrated emission function. (See Appendix A.) The right panel of figure A1 plots $\bar{\Lambda}_m(T, E_x)$ vs. $\log T$ for $E_x = 0.3$, 1, and 2 keV, with the dashed lines comparing the corresponding Boltzmann model fits for $T_x = 1.5$, 7 and 20 MK. The left and right panels of figure 5 respectively use T_x =1.5 MK and E_x =0.3 keV, giving, as noted, very similar characterizations of the radius and time variation of the associated X-ray emission.

Further integration of (30) over radius give the full volume-integrated X-ray luminosity above the given threshold $L_x(t) = L_{E_x}(t)$. The left panel of figure 7 plots this vs. time. The semi-regular episodes of shock-formation and infall lead to a roughly factor 2 variation about the time-averaged value, $\langle L_x \rangle \approx 67\, L_\odot$, computed over the interval $t = 500 - 3000$ ks after the initial shock evolution has settled to its quasi-steady state. The right panel of figure 7 plots the time-averaged luminosity spectrum $L_x(E)$ vs. $\log E$. The black and red curves compare results with and without IC cooling. The overall effect is to reduce the hard X-rays, and so soften the spectrum, with however little change in the total emission, which is strongest at lower energies.

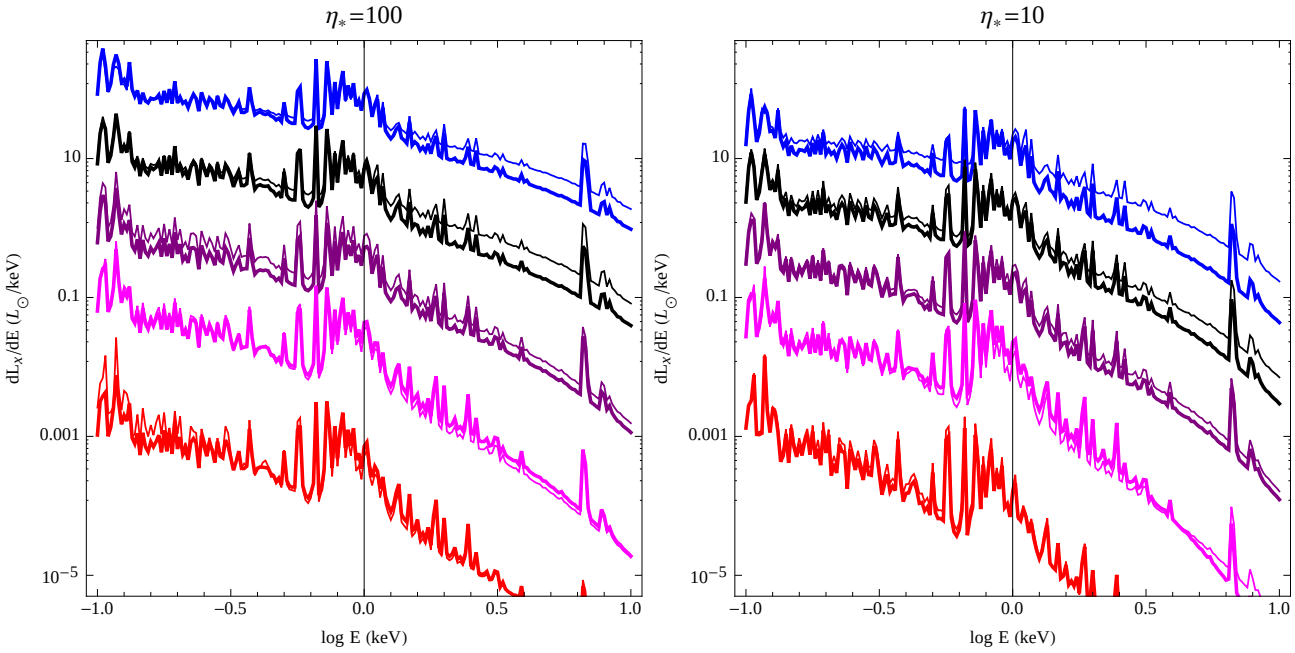

Figure 8. *Left:* Time-averaged luminosity spectra $L_x(E)$ vs. log E for $\eta_* = 100$ models, plotted on a log scale in units of $L_\odot$ for the full series of 5 models with cooling efficiencies $\epsilon_c = 10^{-3}$ (lowermost curves, in red) to 10^{+1} (top, in blue) in steps of 1 dex. The thick line curves include IC cooling, while the thinner curves are for radiative cooling only. *Right:* Same as left panel, but for $\eta_* = 10$. Since EM $\sim \dot{M}^2$, and the ϵ_c is a proxy for $\dot{M}$, the L_x values are scaled here by ϵ_c^2 from what is derived from the numerical computation with the fixed parameters of the standard model shown by the black curves.

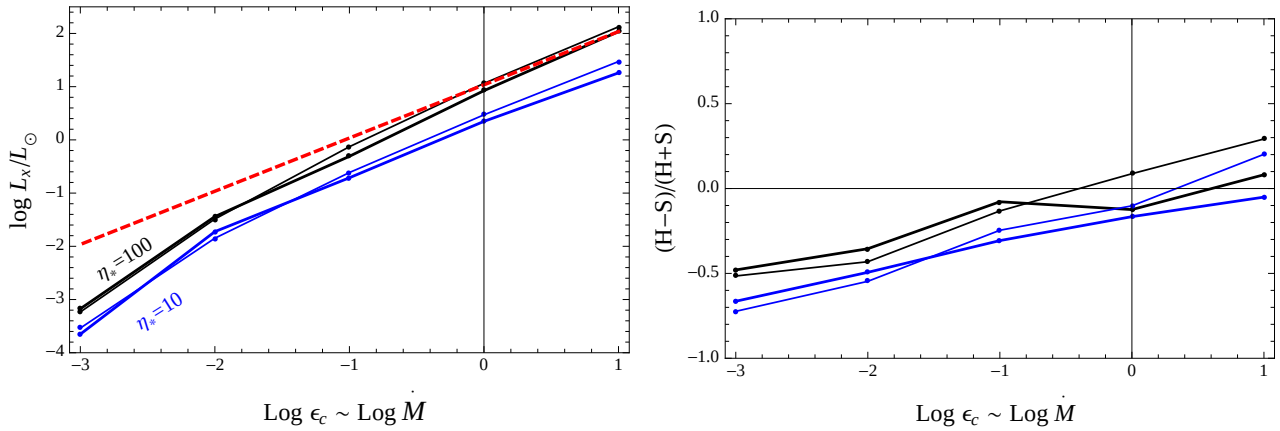

Figure 9. *Left:* Log of time-averaged X-ray luminosity, log L_x, for X-rays above $E_x = 0.3$ keV, plotted vs. log of cooling efficiency log ϵ_c, which acts as a proxy for mass loss rate $\dot{M}$. The upper (black) and lower (blue) curves are respectively for η_* =100 and $\eta_* = 10$, and the thick and normal thickness lines represent models with and without IC cooling. The dashed red line shows a linear relation normalized to values for the $\eta_* = 100$ model with the strongest cooling $\epsilon_c = 10$. *Right:* Analogous plots of hardness ratio (H-S)/(H+S) vs. log ϵ_c, where H represents emission from 1 to 10 keV, and S represents emission from 0.3 to 1 keV.

4 PARAMETER STUDY FOR COOLING EFFICIENCY

4.1 Varying cooling efficiency as a proxy for variations in $\dot{M}$ and L

Let us now examine results from an extensive parameter study of MHD simulations with radiative and IC cooling designed to examine how variations in cooling efficiency affect the X-ray emission.

To study the effect on cooling for a lower $\dot{M}$ that would be expected from lower luminosity stars, we simply reduce the cooling efficiency in our standard stellar wind model by some fixed factor, ϵ_c, where our study spans a grid of 5 cases with $\epsilon_c = 10^{-3}$ to 10^{+1} in steps of 1 dex. In essence, this mimics the effect of changing $\dot{M}$ by ϵ_c, while allowing us to keep the magnetic confinement η_* constant without adjusting the actual field strength. It also avoids the complications of secondary changes in, .e.g., the stellar radius or mass, that would be associated with actual changes in $\dot{M}$ in real stars. (Note that we have included higher ϵ_c to study the strong cooling limit, even though there are no known magnetic stars with mass loss 10 times the standard ζ Pup-like case.)

In models that include IC cooling, we accordingly modify its efficiency by ϵ_c^α, where $\alpha = 0.6$ is the CAK exponent. This is because IC cooling scales with luminosity $L \sim \dot{M}^\alpha$. Because this is

weaker than the $\dot{M}$ scaling of radiative cooling, IC is formally the stronger cooling mechanism for lower-luminosity stars. Moreover, in contrast to radiative cooling, which for higher shock temperatures T_s is reduced by $1/T_s^2$, IC cooling is *independent* of T_s, and so it tends to be particularly effective in getting cooling started. But as the shock cools, radiative cooling takes over, and so it can never be neglected.

Overall, as shown for the above standard case, IC cooling can reduce the DEM at the highest temperatures; but because its scaling with luminosity generally trends in the same sense as the mass loss scaling of radiative cooling, adding IC has only a modest overall effect on the DEMs and X-ray spectra compared to corresponding models with only radiative cooling.

4.2 Results

This limited effect of IC cooling is demonstrated clearly by the plots in figure 8 of time-averaged X-ray spectra. The thick line curves and the regular thickness curves compare directly models with and without IC cooling, for the full set of 5 cooling efficiencies ranging from high ($\epsilon_c = 10$; blue curves at top) to low ($\epsilon = 10^{-3}$; red curves at bottom), and for confinement parameters $\eta_* = 100$ (left) and $\eta_* = 10$ (right). The principal effect is to modestly reduce the high-energy emission for all cases, leading to generally softer X-ray spectra. The strong cubic increase of radiative cooling with shock speed (eqn. (12)) means the radiative cooling is inefficient in the strongest shocks, but the addition of IC cooling, which is independent of shock speed, can still effectively cool such strong shocks, and thus reduce the hard X-ray emission they produce. This effect of IC cooling in dissipating strong shocks, and so reducing and softening the X-ray emission, follows qualitatively the trends predicted by White & Chen (1995) in the context of colliding stellar winds. But for X-rays from MCWS we see here that the overall importance of such effects is quite limited, and that to a reasonable approximation *one can largely ignore IC effects for modeling X-rays from magnetic stars.*

Figure 9 shows how changes in the cooling efficiency ϵ_c affect both the total X-ray luminosity L_x above some threshold $E_x = 0.3\,$keV (left) and the hardness ratio (H-S)/(H+S) (right), where H represents hard X-rays from 1 to 10 keV and S represents soft X-rays between 0.3 and 1 keV. The main trends are that lower efficiency (and so lower mass loss rate) lead toward lower luminosity and lower hardness. The similarity between models with and without IC cooling (shown respectively by thick vs. thin curves) again illustrates the limited importance of IC cooling, except for the tendency toward somewhat softer spectrum in the high-mass-loss radiative-shock limit, vs. somewhat harder spectra in the low-mass-loss, shock-retreat limit.

4.3 Mosaic of radius-time plots for X-ray emission

Finally, to gain insight on how this general shock-retreat scaling is maintained within the complex, time-dependent patterns of shock formation, cooling, and infall that occurs in the full MHD simulations, let us examine again the time and radius variation of the latitudinally integrated X-ray emission that was introduced in the right panel of figure 5.

Figure 10 shows a mosaic of analogous time-radius plots of X-ray emission for various values of the cooling efficiency ϵ_c (in columns) and for the two magnetic confinement cases (top and bottom rows). Within the complex variations from cycles of shock-formation and infall, note the broad patterns and trends for the characteristic height of X-ray emission. Specifically, in cases with lower efficiency, X-rays generally form at lower radii, reflecting the strong shock retreat. The extent and strength of X-ray emission is greater in the model with stronger confinement, η_*=100.

5 ANALYTIC "XADM" SCALING FOR L_X

5.1 X-rays from confined loops with shock retreat

To help interpret these MHD results for X-rays, let us use a semi-analytic analysis to derive a generalized "XADM" scaling law for X-rays emitted from MCWS in slowly rotating magnetic massive stars with dynamical magnetospheres. For this we first note that, as shown in Owocki & ud-Doula (2004), for a dipole magnetic field that intercepts the stellar surface at a co-latitude $\theta_* \equiv \arccos \mu_*$, the local latitudinal variation of radial mass flux $\dot{m}$ (measured relative to the mass loss rate $\dot{M}$ in the non-magnetic case) scales as[4]

$$\frac{d\dot{m}}{d\mu_*} = \mu_B^2 = \frac{4\mu_*^2}{1+3\mu_*^2}\,, \tag{32}$$

where μ_B is the radial projection cosine of the local surface field, and the second equality applies to a standard dipole. The maximum radius r_m of the overlying dipole loop line occurs at the magnetic equator $\mu = 0$, given in terms of the stellar radius R_* by

$$r_m = \frac{R_*}{1-\mu_*^2}\,. \tag{33}$$

In terms of the total kinetic energy of the non-magnetized wind $L_{kin} = \dot{M} V_\infty^2/2$, the associated latitudinal distribution of shock-dissipated energy can be written in terms of the scaled shock speed w_s,

$$\frac{dK_s}{d\mu_*} = \frac{d\dot{m}}{d\mu_*} w_s^2 = \frac{4\mu_*^{2+4\beta}}{1+3\mu_*^2}\left(\frac{w_s}{w_m}\right)^2\,. \tag{34}$$

Following the analysis in §2.5 of Kee et al. 2014, we can write the fraction of this energy emitted as X-rays above a threshold energy E_x as

$$f_x(T_s, E_x) = \int_0^{T_s} \frac{\bar{\Lambda}(T, E_x)}{\Lambda(T)}\,\frac{dT}{T_s}\,, \tag{35}$$

where the post-shock temperature $T_s = w_s^2 T_\infty$, with T_∞ given by eqn. (10) for $v_w = V_\infty$. Using the analysis in Appendix A, this can be approximated by

$$f_x(T_s, E_x) \approx \int_0^{T_s} e^{-E_x/kT}\,\frac{dT}{T_s} \tag{36}$$

$$= e^{-E_x/kT_s} + \frac{E_x}{kT_s}\,\mathrm{E_i}(-E_x/kT_s)\,, \tag{37}$$

where $\mathrm{E_i}$ is the exponential integral. The maximum shock temperature occurs for shocks at the full wind terminal speed, given by eqn. (10) as $kT_\infty = 1.2\,V_8^2\,$keV. Thus if we define the X-ray energy ratio,

$$\epsilon_{xs} \equiv \frac{E_x}{kT_\infty} = \frac{E_x}{1.2\mathrm{keV}\,V_8^2}\,, \tag{38}$$

then the variation of X-ray fraction f_x depends on the reduced shock speed through $E_x/kT_s = \epsilon_{xs}/w_s^2$.

[4] The normalization here accounts for equal contributions from both north and south hemispheres, over an assumed restricted range, $0 < \mu_* < 1$.

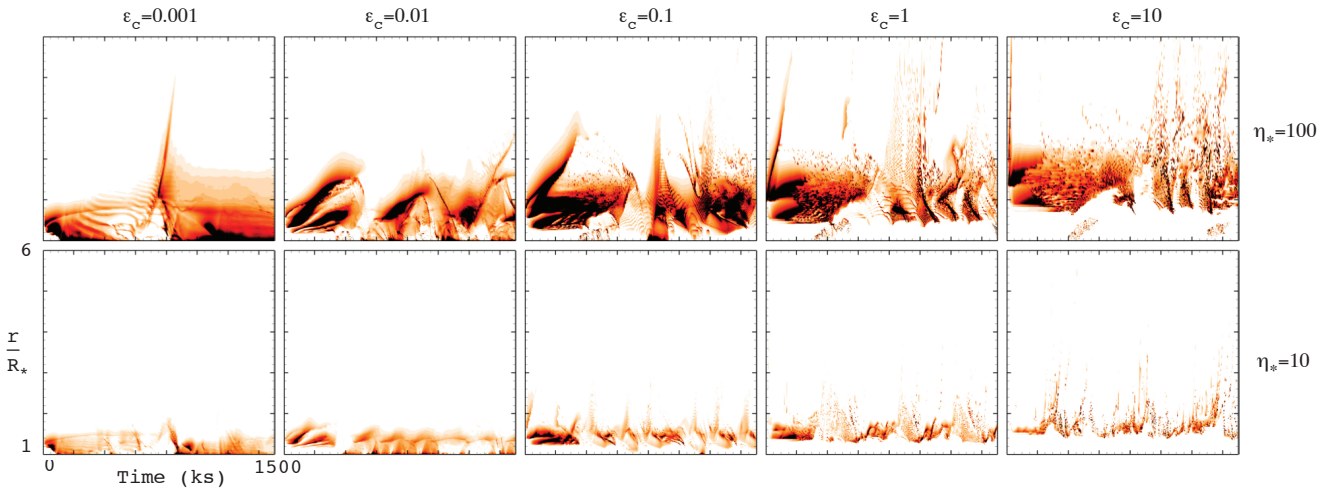

Figure 10. Mosaic of the radius and time variation of latitudinal- and energy-integrated X-ray emission above a threshold $E_x = 0.3$ keV for models with IC cooling and η_*=100 (upper row) or η_*=10 (lower row), with columns representing the 5 values of cooling efficiency ϵ_c, ranging from 10^{-3} (left) to 10^{1} (right). Between the η_*=10 vs. 100 models, the relative color strength reflects the relative X-ray luminosity. Within each η_* row, the emission is scaled by the total L_x for each ϵ_c, and plotted on a common, linear color scale. For decreasing ϵ_c the decrease in the lower boundary radius for X-ray emission reflects the stronger shock retreat, while the higher upper radial extent of X-rays in the $\eta_* = 100$ vs. 10 models reflects the larger Alfvén radius R_A.

For a magnetosphere with closed loops extending over co-latitudes with $0 < \mu_* \leqslant \mu_c$, the ratio of total X-ray luminosity to wind kinetic energy is thus given by the integral,

$$\frac{L_x}{L_{kin}} = \int_0^{\mu_c} \frac{4\mu_*^{2+4\beta}}{1+3\mu_*^2} \left(\frac{w_s}{w_m}\right)^2 f_x(T_s, E_x)\, d\mu_* \,, \qquad (39)$$

where this latitudinal extent can be written in terms of a maximum loop closure radius r_c,

$$\mu_c \equiv \sqrt{1 - R_*/r_c} \,. \qquad (40)$$

Equations (9) and (10) of ud-Doula et al. (2008) give this closure radius in terms of the magnetic confinement parameter,

$$\frac{r_c}{R_*} \approx 0.5 + 0.7(\eta_* + 1/4)^{1/4} \,. \qquad (41)$$

For context, a simple upper limit to the X-ray ratio (39) can be written for the case of strong radiative shocks with $w_s/w_m = f_x = 1$, for which the total dissipated kinetic energy in the magnetosphere is

$$K_s(\eta_*) = \int_0^{\mu_c} \frac{dK_s}{d\mu_*}\, d\mu_* = \int_0^{\mu_c} \frac{4\mu_*^{2+4\beta}}{1+3\mu_*^2}\, d\mu_* \approx C_c \frac{\mu_c^{3+4\beta}}{3+4\beta} \,. \qquad (42)$$

The last approximation ignores the denominator term in the integrand, with C_c an order-unity correction; the resulting power-law form illustrates the strong dependence on closure latitude, i.e. as μ_c^7 for a standard $\beta = 1$ velocity law. The full integration can be evaluated analytically with hypergeometric functions. For $\beta = 1$, the limit of arbitrarily strong confinement $\eta_* \to \infty$, for which $\mu_c \to 1$, gives $K_c = 0.177$, implying then that even in this extreme limit less than 18% of wind kinetic energy is dissipated in MCWS. For the MHD confinement cases $\eta_* = 10$ and 100, the corresponding percentages ($100K_c$%) are 1.5% and 4.7% (see horizontal dashed lines in figure 11).

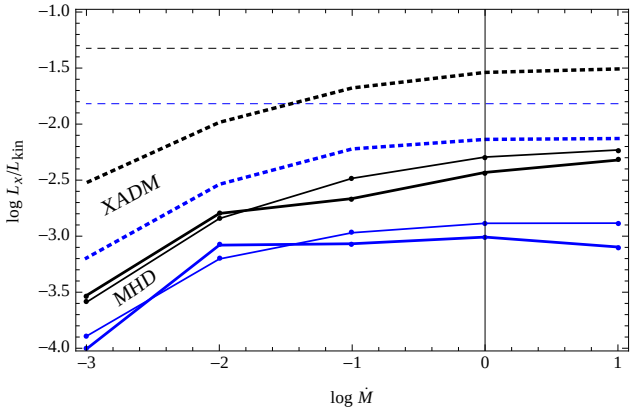

Figure 11. The ratio of total X-ray luminosity L_x from MCWS to the kinetic energy $L_{kin} = \dot{M}V_\infty^2/2$ in the non-magnetized wind, plotted vs. mass loss rate $\dot{M}$ (scaled in terms of the standard model with $\dot{M} = 3.1\times10^{-6} M_\odot$/yr), for cases η_*= 10 (blue) and 100 (black). The heavy and light solid curves are time-averaged values for numerical MHD simulations with and without IC cooling, while the dotted curves are for the XADM analytic scaling in eqn. (39), using the dipole-shock-retreat analysis of Appendix B. The horizontal dashed lines give the upper limits for energy dissipated in MCWS, obtained from eqn. (42) by assuming $w_s/w_m = f_x = 1$ in the analysis leading to eqn. (39). The infall and variability of the full MHD simulations makes the X-ray emission about a factor 5 lower than in the idealized, steady-state XADM model.

5.2 Comparison between analytic and numerical MHD scalings

More generally, computation of the X-ray ratio (39) requires evaluation of the scaled shock speed w_s after accounting for shock retreat, as given by the analysis in §2.5, extended in Appendix B to account for the dipole loop geometry. Using standard root finding,

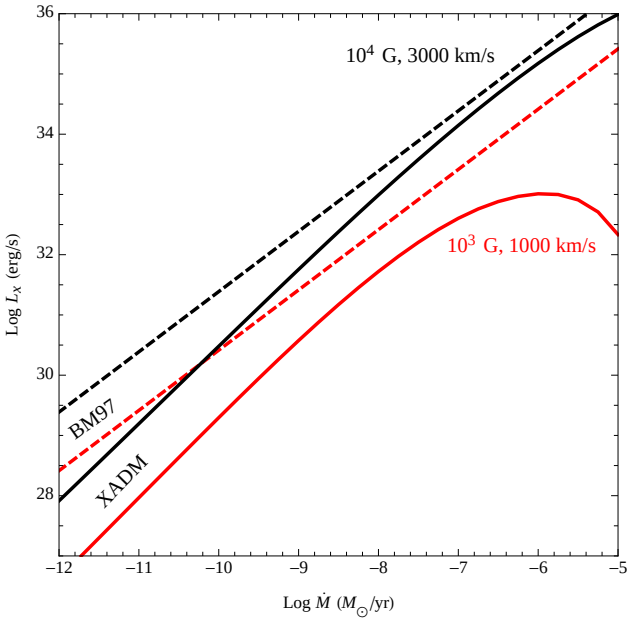

Figure 12. Log-log plot of X-ray luminosity from XADM scaling (39) vs. mass loss rate for a "high" case with large field and fast wind speed ($B_p = 10^4$ G, $V_\infty = 3000$ km/s; black curve), and a "low" case with smaller field and slower speed ($B_p = 10^3$ G, $V_\infty = 1000$ km/s; red curve). The dashed lines compare the corresponding pure power-law scaling suggested by Babel & Montmerle (1997a) (see their eqns. 10 and 11, with $\delta = 1$ and $\epsilon = 1$).

one can readily solve (B16) for w_s for any given values of the cooling efficiency χ_∞ [from eqn. (25)], and loop apex speed w_m.

For a given X-ray energy parameter ϵ_{xs}, this then also gives the X-ray energy ratio, $E_x/kT_s = \epsilon_{xs}/w_s^2$, and so the X-ray fraction f_x through (37). Since $w_m = \mu_*^2$, w_s and thus f_x can be readily evaluated in carrying out the μ_* integral (39), with the integral upper bound μ_c depending on η_* through eqns. (40) and (41).

The upshot is that the value of L_x/L_{kin} is entirely set by the 3 dimensionless parameters η_*, χ_∞, and ϵ_{xs}.

Evaluating (39) in this way, figure 11 plots this semi-analytic scaling for L_x/L_{kin} vs. $\dot{M}$ for $\eta_* = 10$ and 100 (lower and upper dotted curves); the thick and thin solid curves show analogous time-averaged X-ray emission for MHD simulations with and without IC cooling.

The XADM scaling follows a very similar trend to the full MHD simulation results, but is about a factor 5 higher. Compared to the idealized steady-state emission of the analytic XADM model, the numerical simulations show an extensive time variability with repeated intervals of infall of cooled, trapped material, and it appears this lowers the overall efficiency of X-ray emission to about 20% of the idealized XADM prediction.

5.3 Scaling recipe for interpreting observed X-rays

Notwithstanding this overall difference in X-ray efficiency, the good general agreement in the trends for the MHD and XADM encourages application of this semi-analytic XADM scaling to analyze the X-ray emission from magnetospheres with a broader range of magnetic and stellar properties than considered in the detailed MHD simulations here.

The model X-ray luminosity L_x can be obtained by simple numerical evaluation of the integral formula (39), using the auxiliary eqns. (B16), (37), (40), and(41), and then multiplying this by the wind kinetic energy $L_{kin} = \dot{M} V_\infty^2/2$.

As noted, this integral evaluation depends on three dimensionless parameters, namely: the magnetic confinement parameter η_* [defined in eqn. (1)]; the cooling parameter χ_∞ [defined in eqn. (25)]; and ratio of X-ray energy to terminal speed shock energy ϵ_{xs} [defined in eqn. (38)].

These in turn just depend on four physical parameters: the surface field strength B, the stellar radius R_*, and the mass loss rate $\dot{M}$ and terminal speed V_∞ that would occur in a *non*-magnetic stellar wind for the inferred stellar parameters (i.e., luminosity L and mass M).

The upshot is that for any slowly rotating magnetic massive star with an observed large-scale dipole field, estimating the stellar radius and mass loss parameters allows one to use this semi-analytic scaling (39) to predict an X-ray luminosity from MCWS, and then compare this against observed values to test the applicability this MCWS paradigm.

Figure 12 plots L_x vs. $\dot{M}$ (on a log-log scale) for two cases intended to roughly bracket the range in X-ray emission, namely a "high" case with large field and fast wind speed ($B_p = 10^4$ G, $V_\infty = 3000$ km/s; black curve) and a "low" case with smaller field and slower speed ($B_p = 10^3$ G, $V_\infty = 1000$ km/s; red curve). The dashed lines compare the pure power-law scaling suggested by Babel & Montmerle (1997a),

$$L_x = 2.6 \times 10^{30} \mathrm{erg\,s^{-1}}\, \dot{M}_{-10}\, V_8\, B_3^{0.4}\,, \qquad (43)$$

where $\dot{M}_{-10} \equiv \dot{M}/(10^{-10}\, M_\odot/\mathrm{yr})$ and $B_3 \equiv B_p/10^3$ G. Remarkably, the two scalings are quite comparable at moderate mass loss rate. But at low $\dot{M}$ the shock retreat causes the semi-analytic X-rays to drop more steeply than the linear $\dot{M}$ scaling assumed by BM97a. Moreover, at high $\dot{M}$, the reduction of magnetic confinement (to η_* approaching unity) for the case with lower field (B_p =1000 G) causes a flattening and even turnover in L_x, again making this fall well below the linear scaling for BM97a.

This demonstrates quite clearly the importance of both shock retreat and magnetic confinement in setting the mass-loss scaling of X-ray luminosity from MCWS. In applying this XADM scaling to interpreting X-ray observations, it would be appropriate to reduce the predicted L_x by an efficiency factor ~ 0.2 to account for lower average emission from dynamical models with infall of trapped material.

6 SUMMARY & FUTURE WORK

This paper uses MHD simulations to examine the effects of radiative and inverse-Compton (IC) cooling on X-ray emission from magnetically confined wind shocks (MCWS) in the dynamical magnetospheres (DM) that arise in slowly rotating magnetic massive stars with radiatively driven (CAK) stellar winds. The key results can be summarized as follows:

- The scaling of IC cooling with luminosity and radiative cooling with mass loss rate suggests that for CAK winds with $\dot{M} \sim L^{1.7}$, IC cooling should become relatively more important for lower luminosity stars. However, because the sense of the trends is similar, including IC cooling has a quite modest overall effect on the broad scaling of X-ray emission.
- For the two fixed values of magnetic confinement (η_*=10, 100) used in MHD simulations here, the reduced efficiency of radiative cooling from a lower mass loss rate causes a shock retreat to

lower speed wind, leading to weaker shocks. This lowers and softens the X-ray emission, making the $\dot{M}$ dependence of L_x steeper than the linear scaling seen at higher $\dot{M}$ without shock retreat.

- These overall scalings of time-averaged X-rays in the numerical MHD simulations are well matched by the L_x computed from a semi-analytic "XADM" model that accounts for both shock retreat and magnetic confinement within the context of steady feeding of the DM by a CAK wind with field-adjusted mass flux. However, the values of L_x are about a factor 5 lower in the MHD models, mostly likely reflecting an overall inefficiency of X-ray emission from the repeated episodes of dynamical infall.
- Comparison with the previous power-law scaling ($L_x \sim \dot{M} V_\infty B^{0.4}$) suggested by BM97a shows a general agreement with XADM at intermediate $\dot{M}$. But the XADM L_x drops well below the power-law scaling at both low $\dot{M}$ (due to shock retreat) and high $\dot{M}$ (due to weakened magnetic confinement).
- The XADM reproduction of trends in MHD X-rays encourages application of this XADM scaling, with a factor 0.2 efficiency reduction, toward interpreting X-ray observations of slowly rotating magnetic massive stars with a broader range of field strength and wind parameters than considered in the MHD simulations here.

Within this theoretical framework, one focus of our future work will be to apply these results toward interpreting X-ray observations for the subset of confirmed magnetic massive stars (Petit et al. 2013) with available X-ray data from *Chandra* or *XMM-Newton*, with initial emphasis on slowly rotating O and B stars. (See Nazé et al. (2014).) To facilitate analysis of the moderately fast rotating B-stars with centrifugal magnetospheres (CM), we also plan an extension of the present simulation study to examine the potential effects of rotation on the X-ray emission.

ACKNOWLEDGMENTS

Support for this work was provided by NASA through Chandra Award numbers TM4-15001A, TM4-1500B and TM4-15001C issued by the Chandra X-ray Observatory Center which is operated by the Smithsonian Astrophysical Observatory for and behalf of NASA under contract NAS8-03060. This work was also carried out with partial support by NASA ATP Grants NNX11AC40G and NNX08AT36H S04, respectively to the University of Delaware and the University of Wisconsin. D.H.C. acknowledges support from NASA ADAP grant NNX11AD26G and NASA *Chandra* grant AR2-13001A to Swarthmore College. We thank M. Gagné and G. Wade for many helpful discussions. We especially thank C. Russell for providing us tabulations of the radiative emission function $\Lambda(E,T)$ through his application of the APEC model in XSPEC.

REFERENCES

Arnaud K. A., 1996, in Jacoby G. H., Barnes J., eds, Astronomical Data Analysis Software and Systems V Vol. 101 of Astronomical Society of the Pacific Conference Series, XSPEC: The First Ten Years. p. 17

Babel J., Montmerle T., 1997a, ApJ, 485, L29

Babel J., Montmerle T., 1997b, A&A, 323, 121

Castor J. I., Abbott D. C., Klein R. I., 1975, ApJ, 195, 157

Chlebowski T., Harnden Jr. F. R., Sciortino S., 1989, ApJ, 341, 427

Drew J. E., 1989, ApJS, 71, 267

Foster A. R., Ji L., Smith R. K., Brickhouse N. S., 2012, ApJ, 756, 128

Friend D. B., Abbott D. C., 1986, ApJ, 311, 701

Gagné M., 2011, *Four Decades of Research on Massive Stars*, ASP Conf. Ser.

Gagné M., Oksala M. E., Cohen D. H., Tonnesen S. K., ud-Doula A., Owocki S. P., Townsend R. H. D., MacFarlane J. J., 2005, ApJ, 628, 986

MacDonald J., Bailey M. E., 1981, MNRAS, 197, 995

Nazé Y., Broos P. S., Oskinova L., Townsley L. K., Cohen D., Corcoran M. F., Evans N. R., Gagné M., Moffat A. F. J., Pittard J. M., Rauw G., ud-Doula A., Walborn N. R., 2011, ApJS, 194, 7

Nazé Y., Petit V., Rinbrand M., Cohen D., Owocki S.and ud-Doula A., Wade G., 2014, MNRAS, submitted

Owocki S., 2004, in Heydari-Malayeri M., Stee P., Zahn J.-P., eds, EAS Publications Series Vol. 13 of EAS Publications Series, Stellar wind mechanisms and instabilities. pp 163–250

Owocki S. P., Sundqvist J. O., Cohen D. H., Gayley K. G., 2013, MNRAS, 429, 3379

Owocki S. P., ud-Doula A., 2004, ApJ, 600, 1004

Pauldrach A., Puls J., Kudritzki R. P., 1986, A&A, 164, 86

Petit V., Owocki S. P., Wade G. A., Cohen D. H., Sundqvist J. O., Gagné M., Maíz Apellániz J., Oksala M. E., Bohlender D. A., Rivinius T., Henrichs H. F., Alecian E., Townsend R. H. D., ud-Doula A., MiMeS Collaboration 2013, MNRAS, 429, 398

Schure K. M., Kosenko D., Kaastra J. S., Keppens R., Vink J., 2009, A&A, 508, 751

Smith R. K., Brickhouse N. S., Liedahl D. A., Raymond J. C., 2001, ApJ, 556, L91

Stevens I. R., Blondin J. M., Pollock A. M. T., 1992, ApJ, 386, 265

Stone J. M., Norman M. L., 1992, ApJS, 80, 791

Sundqvist J. O., ud-Doula A., Owocki S. P., Townsend R. H. D., Howarth I. D., Wade G. A., 2012, MNRAS, 423, L21

ud-Doula A., Owocki S. P., 2002, ApJ, 576, 413

ud-Doula A., Owocki S. P., Townsend R. H. D., 2008, MNRAS, 385, 97

ud-Doula A., Owocki S. P., Townsend R. H. D., 2009, MNRAS, 392, 1022

ud-Doula A., Sundqvist J. O., Owocki S. P., Petit V., Townsend R. H. D., 2013, MNRAS, 428, 2723

White R. L., Chen W., 1995, in van der Hucht K. A., Williams P. M., eds, Wolf-Rayet Stars: Binaries; Colliding Winds; Evolution Vol. 163 of IAU Symposium, Theory and observations of non-thermal phenomena in hot massive binaries (Invited). p. 438

APPENDIX A: RADIATIVE EMISSION FUNCTION

X-ray spectra in this paper are computed from the energy- and temperature-dependent emission function $\Lambda(E,T)$, as tabulated from the APEC model (Smith et al. 2001; Foster et al. 2012) in the XSPEC plasma emission code (Arnaud 1996). Figure A1 gives a color plot of $\log \Lambda(E,T)$ vs. the log of energy and temperature.

Integration of this emission function from an energy threshold E_x gives the cumulative function $\bar{\Lambda}(T,E_x)$, with the total cooling function approximated by the value for the lowest tabulated energy, $\Lambda(T) \approx \bar{\Lambda}(T,E_{min})$, where here for tables used $E_{min} = 0.01$ keV. The left panel of figure A2 plots the temperature variation of the ratio $\bar{\Lambda}(T,E_x)/\Lambda(T)$ for $E_x = 0.3$, 1, 2 and 10 keV; the dashed curves show the simple Boltzmann function fits

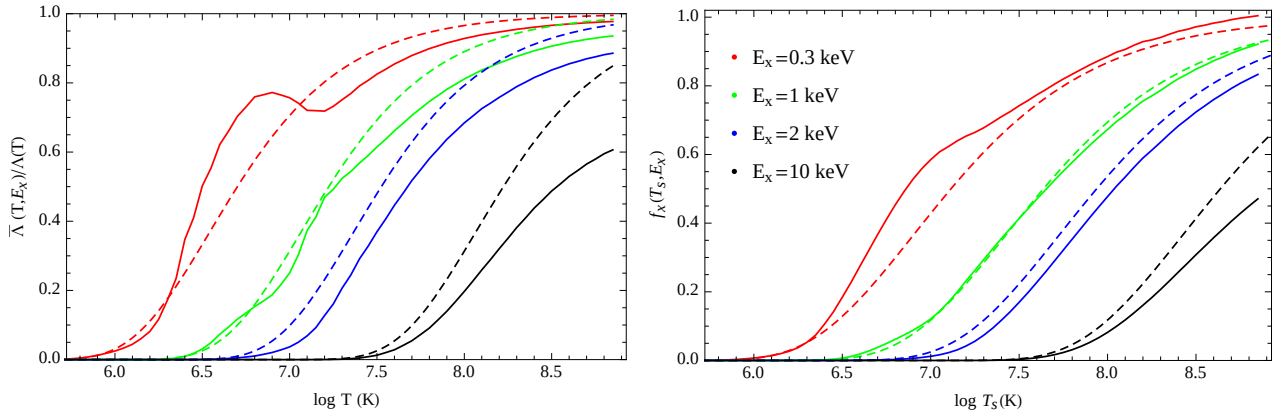

Figure A2. *Left:* Temperature variation of the ratio $\bar{\Lambda}(T, E_x)/\Lambda(T)$ for $E_x = 0.3$, 1, 2 and 10 keV; the dashed curves compare the simple Boltzmann function fits used in the integrand of eqn. (36). *Right:* Associated numerical evaluation of the shock temperature integral (35) for the same four X-ray threshold energies; the dashed curves compare the analytic function in eqn. (37).

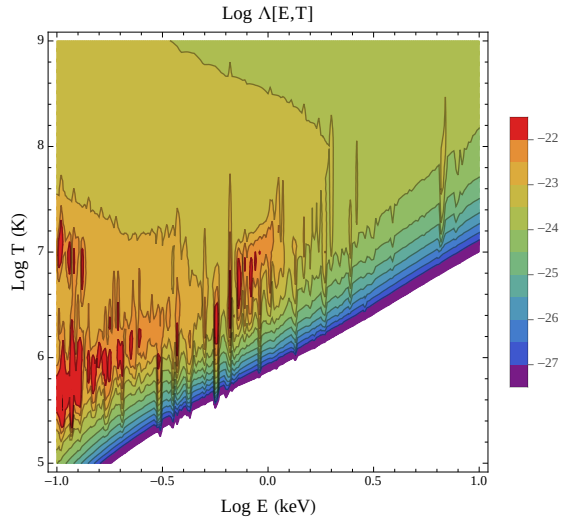

Figure A1. Log of emission function $\Lambda(E, T)$ (erg cm^3/s) in logarithmic energy bins, plotted vs. log of photon energy (in keV) and log temperature (in K).

used in the integrand of eqn. (36). The right panel of plots associated numerical evaluation of the shock temperature integral (35) for the same four X-ray threshold energies; the dashed curves compare the analytic function in eqn. (37).

APPENDIX B: SHOCK RETREAT ALONG A DIPOLE LOOP

Let us now generalize the simplified spherical shock-retreat model of §2.5 to account for the flow geometry along a dipole loop. For a flow tube along a coordinate s with cross sectional area A, we can write eqn. (20) in the generalized form

$$\frac{T^2 dT}{T_s^3} = -\frac{2}{5}\frac{\bar{\mu}\Lambda_m}{kT_s}\frac{\rho T^2}{vT_s^2}\,ds \tag{B1}$$

$$= -\frac{2}{5}\frac{\bar{\mu}\Lambda_m}{kT_s}\frac{\rho^2 T^2}{\dot{M}T_s^2}\,A\,ds \tag{B2}$$

$$= -\frac{32}{5}\frac{\bar{\mu}\Lambda_m}{kT_s}\frac{\rho_{ws}^2 T_s^2}{\dot{M}T_s^2}\,A\,ds \tag{B3}$$

$$= -\frac{512}{15}\frac{\bar{\mu}\Lambda_m}{v_s^2}\frac{\dot{M}}{v_s^2 A_s^2}\,A\,ds \tag{B4}$$

$$= -\frac{1}{\chi_\infty}\frac{\dot{m}}{w_s^4}\frac{A_*}{A_s^2 R_*}\,A\,ds\,, \tag{B5}$$

where $\dot{m}$ allows for a mass loss weighting for a given flow tube, defined as a fraction of the spherical mass loss $\dot{M}$ used in the definition of χ_∞. Integration from the shock radius r_s gives the temperature variation,

$$1 - \left(\frac{T}{T_s}\right)^3 = \frac{3}{\chi_\infty}\frac{\dot{m}}{w_s^4}\frac{A_*}{A_s^2 R_*}\int_{r_s}^{r} A\,ds\,. \tag{B6}$$

Setting the apex temperature $T(r_m) = 0$ then allows us to cast a general implicit equation for the shock radius r_s,

$$g(r_s/r_m) \equiv \int_{r_s/r_m}^{1} \frac{A}{A_m}\frac{ds}{r_m} = \frac{\chi_\infty}{3}\frac{w_s^4}{\dot{m}}\frac{A_s^2}{A_* A_m}\frac{R_*}{r_m}\,. \tag{B7}$$

For the spherical case with $ds = dr$, $A \sim r^2$ and $\dot{m} = 1$,

$$1 - \left(\frac{r_s}{r_m}\right)^3 = \chi_\infty \left(\frac{w_s r_s}{r_m}\right)^4 \frac{r_m}{R_*}\,, \tag{B8}$$

which is equivalent to (23).

For flow along a dipole magnetic field line with base co-latitude set by μ_*, we have

$$\frac{A}{A_*} = \frac{B_*}{B} = \left(\frac{r}{R_*}\right)^3 \frac{\sqrt{1+3\mu_*^2}}{\sqrt{1+3\mu^2}}\,, \tag{B9}$$

where $r = (1-\mu^2)r_m$, and $r_m = R_*/(1-\mu_*^2)$. Also the differential along the field line coordinate can be written

$$ds = \frac{r d\theta}{\hat{B}_\theta} = -\frac{r\sqrt{1+3\mu^2}}{1-\mu^2}\,d\mu\,, \tag{B10}$$

where $\hat{B}_\theta$ is the unit field projection in the θ (latitudinal) direction. Thus

$$g(r_s/r_m) = \int_{r_s/r_m}^{1} \frac{B_m}{B}\,\frac{ds}{r_m} \tag{B11}$$

$$= \int_0^{\mu_s} \left(\frac{r}{r_m}\right)^4 \frac{d\mu}{1-\mu^2} \tag{B12}$$

$$= \int_0^{\mu_s} (1-\mu^2)^3\, d\mu \tag{B13}$$

$$= \mu_s - \mu_s^3 + \frac{3\mu_s^5}{5} - \frac{\mu_s^7}{7}\,, \tag{B14}$$

where $\mu_s \equiv \sqrt{1 - r_s/r_m}$.

As done for spherical shock retreat in §2.5, for a given χ_∞ and $w_m = \mu_*^2$, we can now use this analytic formula (B14) for g to solve for r_s (and, for a $\beta = 1$ law, for $w_s = 1 - R_*/r_s$), through the implicit equations,

$$g(r_s/r_m) = \frac{\chi_\infty}{3}\,\frac{w_s^4}{\dot{m}}\,\frac{B_* B_m}{B_s^2}\,\frac{R_*}{r_m} \tag{B15}$$

$$\mu_s - \mu_s^3 + \frac{3\mu_s^5}{5} - \frac{\mu_s^7}{7} = \frac{\chi_\infty}{6\mu_*}\,\frac{1+3\mu_*^2}{1+3\mu_s^2}\left(\frac{w_s r_s}{r_m}\right)^4 \left(\frac{r_s}{R_*}\right)^2, \tag{B16}$$

where the second equality uses a weighting $\dot{m} = 2\mu_*/\sqrt{1+3\mu_*^2}$ for the mass flux *along* a field line with base latitude set by μ_* (Owocki & ud-Doula 2004).

The solid curves in figure 3 plot the variation of w_s vs. χ_∞ for various loop lines with scaled apex speed w_m from 0.1 to 0.9. The dashed curves compare results for the simplified spherical shock-retreat example of §2.5. The differences only become significant for large χ_∞ (low $\dot{M}$), but for completeness we use this full dipole shock retreat in the XADM scaling analysis of §5.